

LETTERS

Correlation between neural spike trains increases with firing rate

Jaime de la Rocha^{1*}, Brent Doiron^{1,2*†}, Eric Shea-Brown^{1,2}, Krešimir Josić³ & Alex Reyes¹

Populations of neurons in the retina^{1–3}, olfactory system⁴, visual⁵ and somatosensory⁶ thalamus, and several cortical regions^{7–10} show temporal correlation between the discharge times of their action potentials (spike trains). Correlated firing has been linked to stimulus encoding⁹, attention¹¹, stimulus discrimination⁴, and motor behaviour¹². Nevertheless, the mechanisms underlying correlated spiking are poorly understood^{2,3,13–20}, and its coding implications are still debated^{13,16,21,22}. It is not clear, for instance, whether correlations between the discharges of two neurons are determined solely by the correlation between their afferent currents, or whether they also depend on the mean and variance of the input. We addressed this question by computing the spike train correlation coefficient of unconnected pairs of *in vitro* cortical neurons receiving correlated inputs. Notably, even when the input correlation remained fixed, the spike train output correlation increased with the firing rate, but was largely independent of spike train variability. With a combination of analytical techniques and numerical simulations using ‘integrate-and-fire’ neuron models we show that this relationship between output correlation and firing rate is robust to input heterogeneities. Finally, this overlooked relationship is replicated by a standard threshold-linear model, demonstrating the universality of the result. This connection between the rate and correlation of spiking activity links two fundamental features of the neural code.

How do cortical cells transform correlation between their synaptic currents into correlation between their output spike trains? We addressed this question by studying pairwise spike train correlations, a strategy that can capture the full statistical structure of a neural network^{2,3}. Correlated fluctuating currents resembling synaptic activity²³ were injected into the somata of 20 unconnected cortical neurons (see Methods). The input current to cell i ($i = 1, 2$) was:

$$I_i = \mu_i + \sigma_i \left(\sqrt{1-c} \xi_i(t) + \sqrt{c} \xi_c(t) \right) \quad (1)$$

where μ_i is the temporal average of the current. The next term represents gaussian fluctuations with a temporal structure consistent with that *in vivo*²³, and was composed of two weighted factors: ξ_i , which was independent for each cell, and ξ_c , which was common to all cells (Fig. 1a). The input correlation coefficient, c ($0 \leq c \leq 1$), set the relative weight of the shared fluctuations, whereas σ_i set the variance of the total input current. These parameters were adjusted so that the variability and covariability of the membrane potentials²⁴ and spike trains^{7,8} were similar to those observed *in vivo* (Fig. 1b). Typical spike train cross-correlation functions had positive central peaks with short timescales (~ 20 ms; Fig. 1c, left), indicative of spike-time synchrony⁵.

To quantify spike train correlation between two cells, we computed the correlation coefficient^{1,7,8,10} of the spike counts, n_1 and

n_2 , over a sliding window of length T :

$$\rho_T = \frac{\text{Cov}(n_1, n_2)}{\sqrt{\text{Var}(n_1)\text{Var}(n_2)}} \quad (2)$$

where Cov is the covariance and Var the variance. The correlation coefficient ρ_T is a dimensionless quantity ranging between 0 for independent and 1 for fully correlated spike trains. For large T , ρ_T saturates to a value $\rho^{8,10}$ (see Methods).

As expected, ρ_T increased with $c^{14,15,17}$ (Fig. 1d); however, ρ_T was always less than c , indicating that the correlation in the input currents bounds the correlation between the output spikes. Our central and more surprising finding was that ρ_T increased with the output firing rate v when c was fixed (Fig. 1e). We delivered currents with a fixed $c = 0.5$ and various values of μ and σ , thus eliciting spike trains with a range of firing rates and inter-spike interval coefficients of variation (CV). Spike trains with similar v were paired to compute ρ_T . Despite ρ_T increasing strongly with rate it did not depend on the CV (inset Fig. 1e). The same increasing trend holds for all T values examined, and occurred across several identified cell types (see Supplementary Information).

The correlation–rate relationship (Fig. 1e) might be expected owing to an increased probability of spikes occurring close in time at high rates. The coefficient ρ_T corrects for this spurious rate-dependence of correlation, as illustrated by the following example of two cells receiving inputs constructed from three independent Poisson trains x_1 , x_2 and x_c with rates $(1-c)v$, $(1-c)v$ and cv , respectively (Fig. 1f). For a simple model that converts every input spike into an output spike, the output trains $y_1 = x_1 + x_c$ and $y_2 = x_2 + x_c$ have rate v and a correlation that depends on the rate of the common train x_c (Fig. 1f, red spikes). The correlation measured as the average product $\langle n_1 n_2 \rangle = cvT + (vT)^2$ depends on v through: (1) the baseline chance correlation $(vT)^2$, which gives a non-zero correlation even in the case $c = 0$; (2) the scaling of the first term by v , which gives the absolute number of synchronous spikes. The coefficient ρ_T (equation (2)) corrects for these v -dependencies through baseline subtraction and appropriate normalization: $\rho_T = \frac{\langle n_1 n_2 \rangle - \langle n_1 \rangle \langle n_2 \rangle}{\sqrt{(\langle n_1^2 \rangle - \langle n_1 \rangle^2)(\langle n_2^2 \rangle - \langle n_2 \rangle^2)}}$. Specifically, noting $\langle n_i \rangle = vT$ and $\langle n_i^2 \rangle = vT + (vT)^2$ yields $\rho_T = cvT/vT = c$, thus showing how ρ_T does not have a built-in dependence on v . Therefore the correlation–rate relationship exhibited by the data (Fig. 1e) is a priori unexpected, and instead must follow from an input–output property of spiking neurons.

To analyse further the correlation–rate relationship we replaced the *in vitro* neurons with a pair of leaky ‘integrate-and-fire’ (LIF) model neurons²⁵ (see Methods). We fixed μ and σ , and performed simulations of the LIF neuron pair to compute $\rho(c)$. The coefficient c ranged from 0 to 0.3, thus yielding ρ values that are comparable to

¹Center for Neural Science, New York University, New York 10003, USA. ²Courant Institute of Mathematical Sciences, New York University, New York 10012, USA. ³Department of Mathematics, University of Houston, Houston, Texas 77204, USA. [†]Present address: Department of Mathematics, University of Pittsburgh, Pittsburgh, Pennsylvania 15260, USA. *These authors contributed equally to this work.

those measured *in vivo*^{7,8,11}. In this range $\rho(c)$ was approximately linear (Fig. 2a, b), allowing us to use perturbation techniques²⁶ to obtain an expression for $\rho(c)$ (see Supplementary Information):

$$\rho \approx S(\mu, \sigma) c = \frac{\sigma^2 \left(\frac{dv}{d\mu} \right)^2}{CV^2 v} c \quad (3)$$

We define the slope $S(\mu, \sigma)$ relating ρ to c as correlation susceptibility. Here $dv/d\mu$ is the derivative of the spike-rate transfer function (that is, the relationship between firing rate, $v(\mu, \sigma)$, and the mean injected current). Equation (3) accurately predicts the transformation $\rho(c)$ obtained via simulations (Fig. 2a, b, dashed lines).

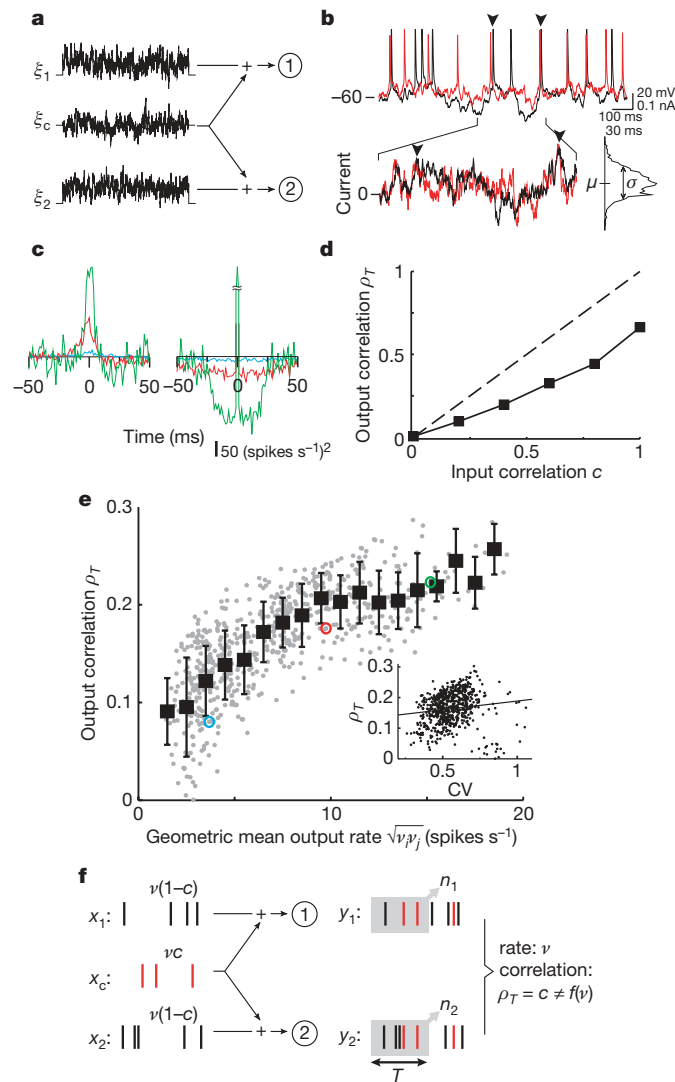


Figure 1 | Relationship between output spike correlation and rate in *in vitro* cells. **a**, Twenty neurons from cortical slices ($n = 11$) were stimulated with gaussian currents (filtered with a time constant of 5 ms), with both common and independent components. **b**, Fluctuating current injection (bottom) often evoked nearly synchronous spikes (top arrowheads). Red and black traces are membrane potentials from cells 1 and 2, respectively. **c**, Typical cross- (left) and auto-correlation (right) functions from a pair of cells firing at low (blue), medium (red) and high (green) rate. **d**, A typical ρ_T versus c for a pair of cells. **e**, The correlation ρ_T in a population ($n = 123$ pairwise comparisons) increases with $\sqrt{v_1 v_2}$ and does not co-vary with $\sqrt{CV_1 CV_2}$ (inset, linear regression, $r = 0.13$); c was fixed at 0.5. Squares represent mean and s.d. of the population, and coloured circles the examples shown in **c**. **f**, A simple cell model that generates an output spike for every input spike. The correlation ρ_T is fixed at c , and is independent of v . Throughout we used $T = 40$ ms.

As with the experiments, we varied μ or σ while keeping c fixed to obtain different values of v . A plot of ρ versus v when μ (or σ) was increased while keeping σ (or μ) fixed (inset of Fig. 2c) shows that ρ rapidly increased in the physiological range of 0–50 spikes s^{-1} and asymptoted to c at high rates (Fig. 2c). Notably, the correlation–rate curves obtained by increasing μ or σ were nearly identical, even though voltage traces, correlation functions and CVs were very different (Fig. 2c). To show that these results did not depend on specific μ and σ values, we used equation (3) to sweep a large region of the μ – σ parameter space. The resultant ρ – v values were confined to a narrow band around the stereotyped curve (Fig. 2c, shaded areas). This allowed us to rewrite equation (3) in an approximate form in which the susceptibility, S , depends only on the output rate and not on the input variables μ and σ :

$$\rho \approx S(v) c \quad (4)$$

The empirically measured ρ_T also increased with v for all T examined; however, the approximation that S depends only on v (equation (4)) becomes progressively less accurate as T decreases (see Supplementary Information).

To determine whether the correlation–rate relationship emerges in a less controlled and more biologically relevant setting, we performed simulations of a two-layer network where neurons from layer 1 were randomly connected to neurons in layer 2 (Fig. 3a). Layer 1 consisted

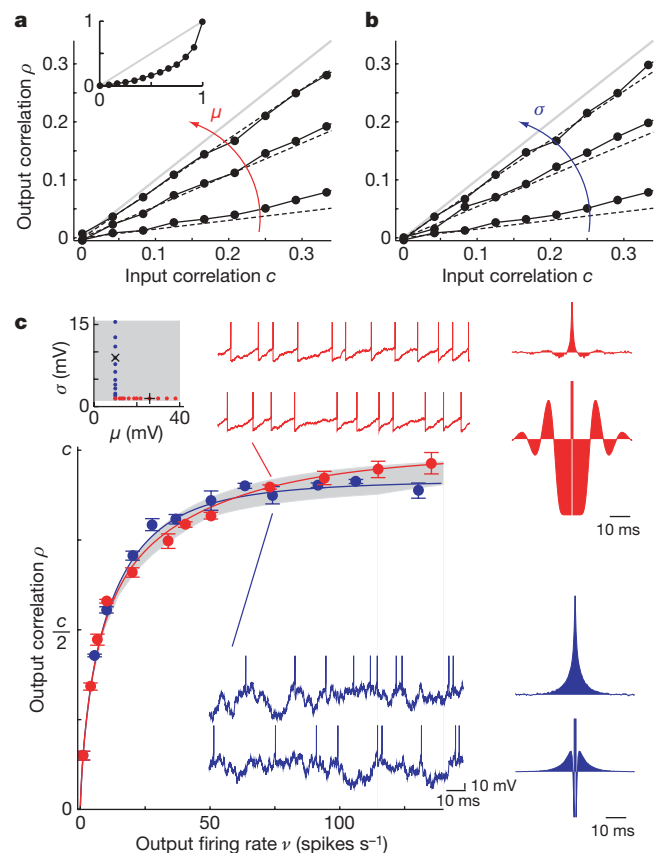


Figure 2 | The correlation–rate relationship in an integrate-and-fire neuron model. **a**, ρ versus c from simulations (solid line) and theory (dashed line, from equation (3)). Increases in either μ (**a**) or σ (**b**) increase the slope of $\rho(c)$. Grey lines are the diagonal $\rho = c$. Inset shows $\rho(c)$ for all c . **c**, As μ (red) or σ (blue) were varied following the paths drawn in the inset, ρ and v co-varied as shown. Note that this relationship holds only when $\rho(c)$ is linear (**a** and **b**). Simulations (dots) and theory (solid line) show a dependence of ρ and v along a stereotyped curve. The shaded area shown in μ – σ space (inset) was swept using equation (3) and yielded the shaded area around the ρ – v curves. Voltage traces, cross- and auto-correlation functions (upper and lower panels, respectively) are illustrated for two sets of (μ, σ) values (see + and x in inset). We used $\tau_m = 10$ ms.

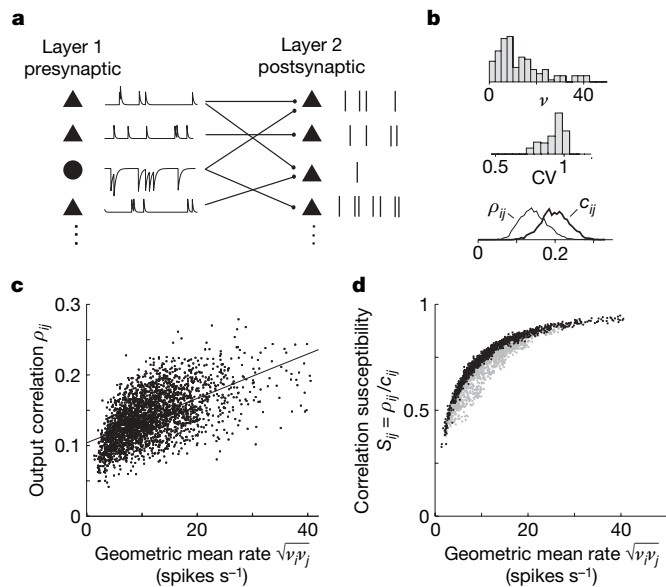


Figure 3 | Correlation-rate relationship in a simple network. **a**, Two-layer network with sparse random connectivity (connection probability was 0.25) where layer 1 contained excitatory and inhibitory cells firing with Poisson statistics. Layer 2 cells were conductance-based LIF neurons with randomly chosen synaptic weights. **b**, Distribution of v (top), CV (middle) and c_{ij} and ρ_{ij} (bottom) across layer 2. **c**, ρ_{ij} versus $\sqrt{v_i v_j}$ for layer 2 (linear regression $r = 0.57$). **d**, $S_{ij} = \rho_{ij}/c_{ij}$ versus $\sqrt{v_i v_j}$ for each pair shown in **c**. Pairs were grouped according to $q_{ij} = v_i/v_j$ (with $v_i \leq v_j$): $q_{ij} > 0.5$ (black) and $q_{ij} \leq 0.5$ (grey).

of excitatory or inhibitory neurons that fired stationary Poisson spike trains with fixed rate, whereas layer 2 neurons were conductance-based LIF model neurons that received randomly weighted AMPA (α -amino-3-hydroxy-5-methyl-4-isoxazole propionic acid) and GABA_A (γ -aminobutyric acid) synapses (see Methods). Each cell i in layer 2 received an input current with a different mean and variance, producing a natural heterogeneity in their firing rates, v_i , and variability, CV _{i} (Fig. 3b). In addition, each pair of layer 2 cells, i and j , shared a different number of afferents, giving rise to a wide distribution of input correlation coefficients, c_{ij} , and in turn a wide distribution of output correlation coefficients, ρ_{ij} (Fig. 3b).

A plot of ρ_{ij} versus the geometric mean of the rates $\sqrt{v_i v_j}$ shows a positive correlation (Fig. 3c). However, the trend is not nearly as tight as the one obtained in the controlled setting (compare Fig. 3c with Fig. 2c), primarily owing to the heterogeneity in c_{ij} (Fig. 3b, bottom panel). After normalization by the measured c_{ij} values (obtainable experimentally using intracellular recordings), we obtained $S_{ij} = \rho_{ij}/c_{ij}$ and a tight clustering of points along the same stereotyped curve emerged (Fig. 3d). If we group the pairs according to how different their rates are, we find that spike trains with similar rates (Fig. 3d, black points) showed slightly larger S_{ij} and a tighter correlation-rate relationship than pairs with more different rates (Fig. 3d, grey points). The same qualitative results were obtained in networks where synapses had slow kinetics (NMDA (N-methyl-D-aspartate) and GABA_B), or where the total conductance was highly non-gaussian (see Supplementary Information).

The experiments, simulations and theory, although showing a clear relationship between ρ and v , do not give a mechanistic understanding of the relationship. To develop this intuition, we examined phenomenological neuron models defined by a simple function, f , that transforms an input random variable, I , with gaussian statistics (μ, σ) to an output random variable, n (Fig. 4a). The inputs I_1 and I_2 to a pair of such neuron models were constructed in analogy to our two-cell system so that their correlation coefficient was c (compare Fig. 1a to Fig. 4a). We varied the mean input, μ , while keeping σ and c fixed (as in Fig. 2c, red curve), and computed the mean output $\langle n \rangle$ and the output correlation coefficient ρ (equation (2)). When f was strictly linear in I (Fig. 4c, top row), then $\rho = c$ for all values of μ , making ρ independent of $\langle n \rangle$. However, when f was threshold-linear, which captures the rectifying property of spike generation, ρ increased with $\langle n \rangle$ (Fig. 4b), as was observed previously (Figs 1e and 2c). The fact that the simple threshold-linear model reproduced the correlation-rate relationship indicates that the specific dynamics of the cell model are not vital to the relationship. Modifying the threshold-linear transfer, to include saturation, produced a non-monotonic relationship between ρ and $\langle n \rangle$ (Fig. 4c, middle row). Similarly, adding a boosting non-linearity to the threshold-linear model introduces a small concavity in the ρ - $\langle n \rangle$ relationship (Fig. 4c, bottom row). Despite this diversity of behaviour across these examples, one general feature is clear: when the input distribution $P(I)$ (coloured gaussians) overlapped with the nonlinear region of f , then ρ was significantly less than c .

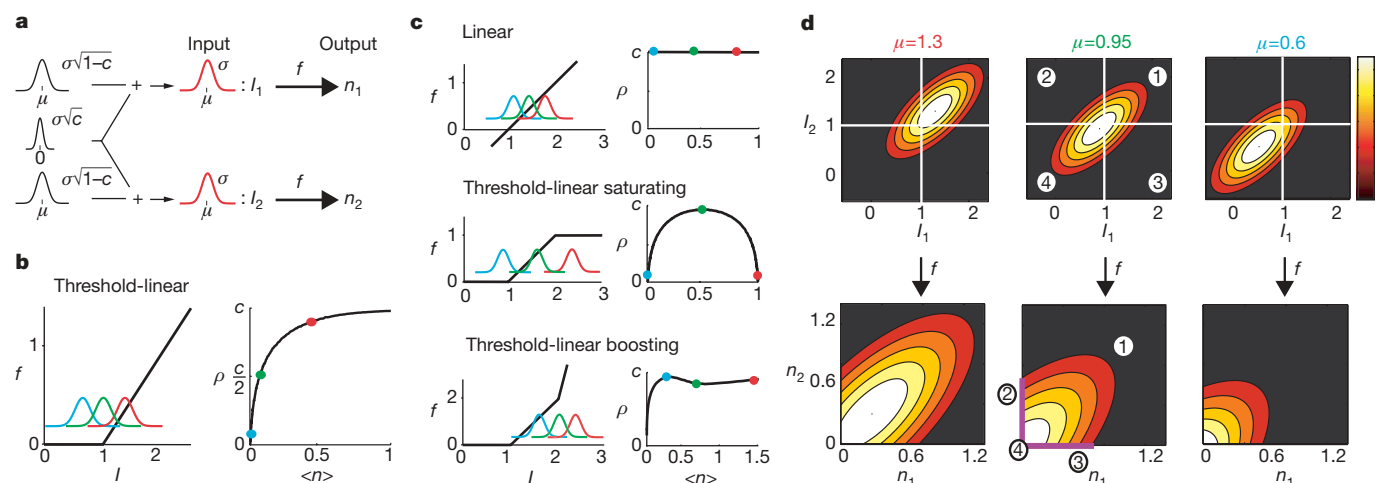


Figure 4 | Nonlinearities shape the correlation-rate relationship in a phenomenological neural model. **a**, The transfer $n_i = f(I_i)$ for a pair of models; note the parallels with Fig. 1a. **b**, f and the ρ - v relationship for the threshold-linear model. Overlaid are the input densities $P(I)$ (coloured gaussians) for three values of μ . **c**, Same as in **b** using three different f functions (see text). **d**, The joint densities $P(I_1, I_2)$ and $P(n_1, n_2)$ for the

threshold-linear model for the three values of μ in **b**. The threshold (white lines) partitions the input plane (I_1, I_2) into four quadrants. $P(I_1, I_2)$ is transformed differently in each quadrant (middle column). In **b-d** we set $\sigma = 0.3$ and the results are valid for c in the interval (0, 0.5), whereas $c = 0.5$ in panel **c**.

For the threshold and saturating nonlinearities this effect was especially prominent as ρ limited to zero.

The correlation between I_1 and I_2 (or n_1 and n_2) is graphically represented as the eccentricity of their joint probability density function, $P(I_1, I_2)$ (or $P(n_1, n_2)$). The eccentricity, loosely defined as the elongation of the probability density function along the diagonal $I_1 = I_2$, increases with correlation. The eccentricity of $P(I_1, I_2)$ is, by construction, uniquely determined by c , so that for $c = 0$ the probability density function has a circular distribution, whereas as c approaches 1 the probability density function becomes increasingly confined to the diagonal. In contrast, the eccentricity of $P(n_1, n_2)$ depends on both c and μ (Fig. 4d, bottom row), as the following analysis using the threshold-linear model shows. The threshold, associated with f , partitions the input plane (I_1, I_2) into four quadrants (Fig. 4d, middle column). In each quadrant, the transformation of $P(I_1, I_2)$ into $P(n_1, n_2)$ via f is different. When μ is large, most of the mass of $P(I_1, I_2)$ is contained in quadrant 1, so that $P(I_1, I_2)$ is mapped approximately linearly to $P(n_1, n_2)$. As a consequence, $P(n_1, n_2)$ inherits much of the eccentricity of $P(I_1, I_2)$ (Fig. 4d, bottom-left panel), implying $\rho \approx c$. As μ decreases, the mass of $P(I_1, I_2)$ is shifted from quadrant 1 to the other three quadrants, and f distorts $P(I_1, I_2)$ so that the eccentricity of $P(n_1, n_2)$, and hence ρ , decreases (Fig. 4d, middle and right panels of bottom row). Thus, as μ is varied both ρ and $\langle n \rangle$ are expected to co-vary, yielding the correlation–rate relationship shown in Figs 1e, 2c and 4b. An analogous description can be made using the spiking LIF model (see Supplementary Information).

The above analysis shows that nonlinearities in the transfer function can cause different v -dependencies of ρ and allows us to explore the effect of other nonlinearities present in neurons. Phenomena such as spike refractoriness (see Fig. 6A of ref. 27), synaptic depression (see Fig. 2A of ref. 28), or dendritic sublinear summation (see Fig. 2 of ref. 29) impose a saturation on rate that would cause the ρ – v relationship to reach a maximum and begin to decrease (Fig. 4c, middle row). Dendritic supra-linear summation (Fig. 4A of ref. 30 and Fig. 2 of ref. 29) introduces boosting effects that would yield small inflections in the ρ – v relationship (Fig. 4c, bottom row). These observations predict that single neuron/synaptic nonlinearities can be an important determinant of network correlation.

A relationship between firing rate and pairwise correlation has, until now, been elusive^{8,10,17,18}. A consequence of the correlation–rate relationship is that, if the firing rate of a population of neurons is tuned to a certain feature (for example, orientation of a bar), the population correlation inherits the same tuning. Consistent with this prediction, ρ_T measured from neurons in primary visual cortex shows a tuning to stimulus orientation when $T < 50$ ms⁸. A direct test of the correlation–rate relationship would require intracellular recordings where measurements of both the afferent current and spike train correlations, as a stimulus is varied, could be obtained²⁴. Nevertheless, analysis of extracellular multi-unit recordings from macaque V1 (A. Kohn and M. Smith, personal communication) and electrosensory receptors (J. Middleton, J. Benda, A. Longtin and L. Maler, personal communication) shows a correlation–rate relationship similar to the one obtained in our network (Fig. 3c), supporting the generality of our result. The correlation–rate relationship prompts a re-examination of rate- and correlation-based coding hypotheses^{8,9,11–13,16,21,22}, because these measures are mechanistically intertwined.

METHODS SUMMARY

Whole-cell somatic recordings were made from layer 5 neurons in slices (300 μ m) from auditory and somatosensory cortices of young mice (postnatal day P14 to P21). Surgical, slicing and recording techniques were done as described previously¹⁹ and followed guidelines established by the NYU Animal Welfare Committee. Computer-generated currents (equation (1); duration $L = 1$ s) were delivered to 1–4 neurons every 1–5 s for a total of $N = 100$ trials. The terms $\xi_i(t)$ and $\xi_c(t)$ were gaussian noises low-pass-filtered with a time constant of 5 ms. The spike count from the i th cell in the k th trial, $n_i^k(t)$, was the number of spikes that occurred in the temporal window $(t, t + T)$. Time was

discretized with $\Delta t = 1.2$ ms. The spike count shift-corrected covariance was:

$$\text{Cov}(n_i, n_j) = \frac{1}{N(L-T)} \sum_{k=1}^N \sum_{t=0}^{L-T} \left(n_i^k(t) n_j^k(t) - n_i^k(t) n_j^{k+1}(t) \right) \quad (5)$$

where the interior sum ranges over time bins. The variance was $\text{Var}(n_i) = \text{Cov}(n_i, n_i)$ and the correlation coefficient ρ_T was computed as in equation (2). In Fig. 1 we used $T = 40$ ms (see Supplementary Information for analysis using $T = 10$ –300 ms).

We used a leaky integrate-and-fire (LIF) neural model²⁵ which obeyed: $\tau_m \frac{dV_i}{dt} = -V_i + \mu + \sigma \sqrt{\tau_m} (\sqrt{1 - c} \xi_i(t) + \sqrt{c} \xi_c(t))$ where V_i is the membrane potential of the i th neuron, and $\tau_m = 10$ ms, threshold = 20 mV and reset = 0 mV. Here $\xi_i(t)$ and $\xi_c(t)$ are white noise currents. Correlation coefficients ρ , defined as the limit of ρ_T as T increases, were estimated from the ratio of the area of the cross-correlation function normalized by the areas of the auto-correlation functions¹⁰ (see Supplementary Information). Other parameters that differ from the experimental data analysis were $L = 100$ s and $\Delta t = 0.5$ ms. The network in Fig. 3 had $N_E = 800$ excitatory and $N_I = 200$ inhibitory cells in layer 1 randomly connected (probability = 0.25) with 100 cells in layer 2. Layer 1 neurons fired Poisson trains with a rate of 10 spikes s^{-1} . Layer 2 neurons were LIF models with conductance-based excitatory and inhibitory synapses with time constants $\tau_E = 4$ ms, $\tau_I = 8$ ms, mean weights $J_E = 0.32$ nS, $J_I = 1.4$ nS and standard deviation $\Delta x = 0.35 J_x$ (where $x = E, I$).

Full Methods and any associated references are available in the online version of the paper at www.nature.com/nature.

Received 16 April; accepted 18 June 2007.

1. Mastronarde, D. N. Correlated firing of cat retinal ganglion cells. I. spontaneously active inputs to x- and y-cells. *J. Neurophysiol.* **49**, 303–324 (1983).
2. Schneidman, E., Berry, M. J., Segev, R. & Bialek, W. Weak pairwise correlations imply strongly correlated network states in a neural population. *Nature* **440**, 1007–1012 (2006).
3. Shlens, J. et al. The structure of multi-neuron firing patterns in primate retina. *J. Neurosci.* **26**, 8254–8266 (2006).
4. Stopfer, M., Bhagavan, S., Smith, B. H. & Laurent, G. Impaired odour discrimination on desynchronization of odour-encoding neural assemblies. *Nature* **390**, 70–74 (1997).
5. Alonso, J. M., Usrey, W. M. & Reid, W. M. Precisely correlated firing in cells of the lateral geniculate nucleus. *Nature* **383**, 815–819 (1996).
6. Bruno, R. M. & Sakmann, B. Cortex is driven by weak but synchronously active thalamocortical synapses. *Science* **312**, 1622–1627 (2006).
7. Zohary, E., Shadlen, M. N. & Newsome, W. T. Correlated neuronal discharge rate and its implication for psychophysical performance. *Nature* **370**, 140–143 (1994).
8. Kohn, A. & Smith, M. A. Stimulus dependence of neuronal correlation in primary visual cortex of the macaque. *J. Neurosci.* **25**, 3661–3673 (2005).
9. deCharms, R. C. & Merzenich, M. M. Primary cortical representation of sounds by the coordination of action potentials. *Nature* **381**, 610–613 (1996).
10. Bair, W., Zohary, E. & Newsome, W. T. Correlated firing in macaque visual area MT: Time scales and relationship to behavior. *J. Neurosci.* **21**, 1676–1697 (2001).
11. Steinmetz, P. N. et al. Attention modulates synchronized neuronal firing in primate somatosensory cortex. *Nature* **404**, 187–190 (2000).
12. Vaadia, E. et al. Dynamics of neuronal interactions in monkey cortex in relation to behavioural events. *Nature* **373**, 515–518 (1995).
13. Abeles, M. *Corticonics: Neural circuits of the cerebral cortex* (Cambridge Univ. Press, New York, 1991).
14. Svirsakis, G. & Hounsgaard, J. Influence of membrane properties on spike synchronization in neurons: theory and experiments. *Network Comput. Neural Syst.* **14**, 747–763 (2003).
15. Galán, R. F., Fourcaud-Trocme, N., Ermentrout, G. B. & Urban, N. N. Correlation-induced synchronization of oscillations in olfactory bulb neurons. *J. Neurosci.* **26**, 3646–3655 (2006).
16. Shadlen, M. N. & Newsome, W. T. The variable discharge of cortical neurons: implications for connectivity, computation, and information coding. *J. Neurosci.* **18**, 3870–3896 (1998).
17. Binder, M. D. & Powers, R. K. Relationship between simulated common synaptic input and discharge synchrony in cat spinal motoneurons. *J. Neurophysiol.* **86**, 2266–2275 (2001).
18. Dorn, J. D. & Ringach, D. L. Estimating membrane voltage correlations from extracellular spike trains. *J. Neurophysiol.* **89**, 2271–2278 (2003).
19. Reyes, A. D. Synchrony-dependent propagation of firing rate in iteratively constructed networks *in vitro*. *Nature Neurosci.* **6**, 593–599 (2003).
20. Doiron, B., Rinzel, J. & Reyes, A. Stochastic synchronization in finite size spiking networks. *Phys. Rev. E* **74**, 030903 (2006).
21. Averbeck, B. B., Latham, P. E. & Pouget, A. Neural correlations, population coding and computation. *Nature Rev. Neurosci.* **7**, 358–366 (2006).
22. Salinas, E. & Sejnowski, T. J. Correlated neuronal activity and the flow of neural information. *Nature Rev. Neurosci.* **2**, 539–550 (2001).
23. Destexhe, A., Rudolph, M. & Paré, D. The high-conductance state of neocortical neurons *in vivo*. *Nature Rev. Neurosci.* **4**, 739–751 (2003).

24. Lampl, I., Reichova, I. & Ferster, D. Synchronous membrane potential fluctuations in neurons of the cat visual cortex. *Neuron* **22**, 361–374 (1999).
25. Ricciardi, L. M. *Diffusion Processes and Related Topics in Biology* (Springer, Berlin, 1977).
26. Lindner, B., Doiron, B. & Longtin, A. Theory of oscillatory firing induced by spatially correlated noise and delayed inhibitory feedback. *Phys. Rev. E* **72**, 061919 (2005).
27. Lau, D. et al. Impaired fast-spiking, suppressed cortical inhibition, and increased susceptibility to seizures in mice lacking kv3.2 K⁺ channel proteins. *J. Neurosci.* **20**, 9071–9085 (2000).
28. Tsodyks, M. V. & Markram, H. The neural code between neocortical pyramidal neurons depends on neurotransmitter release probability. *Proc. Natl Acad. Sci. USA* **94**, 719–723 (1997).
29. Polsky, A., Mel, B. & Schiller, J. Computational subunits in thin dendrites of pyramidal cells. *Nature Neurosci.* **7**, 621–627 (2004).
30. Larkum, M. E., Senn, W. & Lüscher, H.-R. Top-down dendritic input increases the gain of layer 5 pyramidal neurons. *Cereb. Cortex* **14**, 1059–1070 (2004).

Supplementary Information is linked to the online version of the paper at www.nature.com/nature.

Acknowledgements We thank C. Colbert, A. Kohn, L. Maler, D. Nikolic, A.-M. Oswald and A. Renart for their critical reading of the manuscript, and R. Moreno-Bote, M. Schiff and J. Rinzel for insightful discussions. Funding was provided by the Spanish MEC (J.R.), HFSP (B.D.), a Burroughs Wellcome Fund career award and an NSF postdoctoral fellowship (E.S.-B.), NSF (K.J.) and NIH (A.R.).

Author Information Reprints and permissions information is available at www.nature.com/reprints. The authors declare no competing financial interests. Correspondence and requests for materials should be addressed to B.D. (bdoiron@cns.nyu.edu) or J.R. (jrocha@cns.nyu.edu).

METHODS

Experiments. Surgical, slicing and recording techniques were done as described previously¹⁹ and followed guidelines established by the NYU Animal Welfare Committee. Slices were made from auditory and somatosensory cortices of young mice (postnatal day P14 to P21). Whole-cell somatic recordings were made from layer 5 neurons identified under an infrared video microscopy. During recordings, slices (300 μm thick) were perfused at room temperature or at 32 °C with ACSF (with 95% O₂, 5% CO₂). Pipettes were filled with 100 mM K-gluconate, 20 mM KCl, 10 mM phosphocreatine, 10 mM HEPES, 4 mM ATP-Mg, and 0.3 mM GTP at pH 7.3. Filled electrode resistances were in the range of 5 to 10 M Ω and recordings were performed under current-clamp conditions. Voltage and current signals were filtered at 10 KHz and digitized at 5 kHz.

Stimulus protocol. Computer-generated currents (equation (2); duration $L = 1$ s after removing the initial 100 ms) were delivered to 1–4 neurons every 1–5 s. The common $\xi_c(t)$ and the independent terms $\xi_i(t)$ were gaussian noises low-pass-filtered with a time constant of 5 ms. We presented each $N = 100$ trials stimulus block for 1–7 repetitions (see Supplementary Information for details).

Data analysis. Voltage traces were differentiated and action potential times were detected by setting a threshold on the differential traces. The spike trains emitted by the i th cell in the k th trial were represented by a binary time series, $y_i^k(t)$, which equalled 1 if there was a spike at time t and zero otherwise. The spike count, $n_i^k(t)$, was simply the number of spikes that occurred in a window of length T , that is, $n_i^k(t) = \sum_{t'=t}^{t+T} y_i^k(t')$. Time was discretized with $\Delta t = 1.2$ ms resolution and the first 100 ms of the spike trains were removed to correct for spike frequency adaptation. The spike count shift-corrected covariance was computed as:

$$\text{Cov}(n_i, n_j) = \frac{1}{N(L-T)} \sum_{k=1}^N \sum_{t=0}^{L-T} n_i^k(t) n_j^k(t) - \frac{1}{N(L-T)} \sum_{k=1}^N \sum_{t=0}^{L-T} n_i^k(t) n_j^{k+1}(t) \quad (6)$$

where the interior sums range over time bins. Note that in the second term, named the shift-corrector, spike counts from consecutive trials were multiplied. This term equals the product $\langle n_i \rangle \langle n_j \rangle$ for data that are stationary across trials (like in our LIF model) and corrected for both ‘chance correlations’ (baseline correlation expected for independent spike trains) and co-fluctuations due to drifts in the excitability across trials. The variance was obtained by noting that $\text{Var}(n_i) = \text{Cov}(n_i, n_i)$ and the correlation coefficient ρ_T was computed as in equation (2). The analysis shown in Fig. 1 used $T = 40$ ms whereas in the Supplementary Information we explore the range $T = 10$ –300 ms. The output spike shift-corrected cross-correlation function is defined as:

$$C_{ij}(\tau) = \frac{1}{N\Delta t(L-|\tau|)} \sum_{k=1}^N \sum_{t=0}^{L-|\tau|} y_i^k(t) y_j^k(t+\tau) - \frac{1}{N\Delta t(L-|\tau|)} \sum_{k=1}^N \sum_{t=0}^{L-|\tau|} y_i^k(t) y_j^{k+1}(t+\tau) \quad (7)$$

The auto-correlation function was obtained by making $i = j$ in equation (7). Note that, as in the covariance, we have corrected for ‘chance correlations’ in $C_{ij}(\tau)$ by subtracting the corresponding shift-corrector.

Computational model. We used a leaky integrate-and-fire (LIF) neural model²⁵ integrating white noise currents:

$$\tau_m \frac{dV_i}{dt} = -V_i + \mu + \sigma \sqrt{\tau_m} \left(\sqrt{1-c} \xi_i(t) + \sqrt{c} \xi_c(t) \right) \quad (8)$$

where V_i is the membrane potential of the i th neuron, and $\tau_m = 10$ ms, threshold = 20 mV and reset = 0 mV. Correlation coefficients ρ defined as the limit of ρ_T as T increases, were estimated by computing the ratio of the area of the cross-correlation function, $C_{ij}(\tau)$, normalized by the areas of the auto-correlation functions, $C_{ii}(\tau)$ ¹⁰ (see Supplementary Information). Other parameters in the simulations that differ from the data analysis were $L = 100$ s and $\Delta t = 0.5$ ms. ρ in Fig. 2c was numerically obtained from a linear regression of $\rho(c)$ in the interval $c = 0$ –0.12. Parameter values in Fig. 2: $\mu = 10, 14$ and 26 mV, $\sigma = 1.3$ mV (panel a); $\mu = 10$ mV, $\sigma = 1.3, 2.4$ and 8.8 mV (panel b); $\mu = 10$ –38 mV and $\sigma = 1.3$ mV (red in panel c); $\mu = 10$ mV and $\sigma = 1.3$ –15.8 mV (blue in panel c). The theoretical curves in Fig. 2 were computed from standard first passage time formulae appropriate for a LIF neuron receiving white noise inputs²⁵ (see Supplementary Information).

Network simulation. The network in Fig. 3 had $N_E = 800$ excitatory (E) and $N_I = 200$ inhibitory (I) cells in layer 1 and 100 cells in layer 2. Connections were randomly established from layer 1 to layer 2 with a probability $P = 0.25$. Layer 1 cells fired Poisson spike trains at rate $v_E = v_I = 10$ spikes s^{-1} . Each neuron in layer 2 was a LIF neuron model with conductance-based E and I synapses described by:

$$C_m \frac{dV}{dt} = g_L(E_L - V) + g_E(t)(E_E - V) + g_I(t)(E_I - V) \quad (9)$$

$$\frac{dg_\alpha}{dt} = -\frac{g_\alpha}{\tau_\alpha} + \sum_j J_{\alpha,j} \sum_k \delta(t - t_{\alpha,j}^k) \quad (\alpha = E, I) \quad (10)$$

where $\{t^k\}$ are the times of the spikes emitted by the j th pre-synaptic cell and $J_{\alpha,j}$ is the synaptic weight which was zero if the j th cell did not establish a connection or was randomly chosen from a gaussian distribution with mean $J_E = 0.32$ nS ($J_I = 1.4$ nS) and standard deviation $\Delta_\alpha = 0.35 J_\alpha$ ($\alpha = E, I$) if there was one. The synaptic time constants were $\tau_E = 4$ ms, $\tau_I = 8$ ms resembling AMPA and GABA_A kinetics (see Supplementary Information for a slow synapses analysis). We also set threshold = −55 mV, reset = −65 mV, refractory period = 2 ms, membrane capacitance $C_m = 0.12$ nF, leak conductance $g_L = 4.5$ nS, excitatory reversal potential $E_E = 0$ mV, and inhibitory reversal potential $E_I = -80$ mV.